Ammonia-Evaporation-Induced Synthetic Method for Metal (Cu, Zn, Cd, Ni) Hydroxide/Oxide Nanostructures

Yanguang Li, Bing Tan, and Yiying Wu*

Department of Chemistry, The Ohio State University, 100 West 18th Avenue, Columbus, Ohio 43210, U.S.A.

Received March 22, 2007. Revised Manuscript Received October 14, 2007

We report an ammonia-evaporation-induced synthetic method for metal (Ni, Cu, Zn, and Cd) hydroxide/oxide nanostructures including hierarchical CuO spheres with radiating nanoplates, densely branched ZnO nanowires, $Cd(OH)_2$ nanofibers, and $Ni(OH)_2$ nanoplates. One important feature of this mild and surfactant-free methodology is that these nanostructures grow in a dynamic environment with the continuous decrease of pH and ammonia concentration in the solution, which is responsible for the formation of the complex architectures. The obtained $Cd(OH)_2$ nanofibers and $Ni(OH)_2$ nanoplates can also be converted into oxides by a subsequent thermal treatment. In addition to the synthesis and mechanism studies, we have investigated the electrochemical reactivity of the CuO spheres, CdO nanofibers, and NiO nanoplates toward lithium and demonstrated their potential application as anode materials for lithium ion batteries.

Introduction

In recent years there has been great research interest in the synthesis of nanostructured transition metal hydroxide/oxide materials because of their important technological applications. For example, ZnO is a wide band gap n-type semiconductor with large exciton binding energy[1a] and can be used in optoelectronics,[1b] gas sensing,[1c] and photovoltaics.[1d] Co_3O_4 is a p-type magnetic material with applications in lithium ion batteries,[2a] gas sensing,[2b] and electrochromic devices.[2c] CdO has been used as the base material for transparent conductive oxides with high carrier mobilities.[3] CuO has been widely exploited in heterogeneous catalysis,[4a] gas sensing,[4b] and field emission.[4c] $Cd(OH)_2$,[5a] $Ni(OH)_2$,[5b] and NiO[2a] are important energy materials. For applications such as sensing, photovoltaics, and energy storage, nanostructured materials are generally desired because they have the advantages of a high surface area and enhanced chemical/electrochemical activities.

Many methodologies have been developed for the synthesis of nanostructured transition metal oxides. For example, by the thermal evaporation−condensation method or the vapor–liquid–solid method, single-crystalline CuO nanowires,[6a] CdO nanobelts and nanosheets,[6b] ZnO nanowires,[1b,6c] nanobelts,[6b] nanocombs,[6d] and other morphologies[7] have been synthesized. Surfactant-controlled crystal growth by solution reactions is also an important strategy for oxide and hydroxide nanomaterials, and a rich variety of morphologies have been reported in the literature.[8–10] In addition, porous anodic alumina and other porous materials have been used for templated growth of nanowires and nanotubes.[11a] ZnO,[11b] $Ni(OH)_2$,[11c] and Co_3O_4[2b] nanowires and nanotubes have been prepared with a sol–gel reaction in the confined space. Virus-templated synthesis of Co_3O_4 nanowires has also been reported.[12]

* Corresponding author. Phone: (+1) 614-247-7810. Fax: (+1) 614-292-1685. E-mail: wu@chemistry.ohio-state.edu.

(1) (a) Klingshirn, C. *Phys. Status Solidi B* **1975**, *71*, 547. (b) Huang, M. H.; Mao, S.; Feick, H.; Yan, H.; Wu, Y.; Kind, H.; Weber, E.; Russo, R.; Yang, P. *Science* **2001**, *292*, 1897. (c) Rao, G. S. T.; Rao, D. T. *Sens. Actuators, B* **1999**, *B55*, 166. (d) Law, M.; Greene, L. E.; Johnson, J. C.; Saykally, R.; Yang, P. *Nat. Mater.* **2005**, *4*, 455.

(2) (a) Poizot, P.; Laruelle, S.; Grugeon, S.; Dupont, L.; Tarascon, J. M. *Nature* **2000**, *407*, 496. (b) Li, W.; Xu, L.; Chen, J. *Adv. Funct. Mater.* **2005**, *15*, 851. (c) Maruyama, T.; Arai, S. *J. Electrochem. Soc.* **1996**, *143*, 1383.

(3) Yang, Y.; Jin, S.; Medvedeva, J. E.; Ireland, J. R.; Metz, A. W.; Ni, J.; Hersam, M. C.; Freeman, A. J.; Marks, T. J. *J. Am. Chem. Soc.* **2005**, *127*, 8796.

(4) (a) Reitz, J. B.; Solomon, E. I. *J. Am. Chem. Soc.* **1998**, *120*, 11467. (b) Chowdhuri, A.; Gupta, V.; Sreenivas, K.; Kumar, R.; Mozumdar, S.; Patanjali, P. K. *Appl. Phys. Lett.* **2004**, *84*, 1180. (c) Hsieh, C.; Chen, J.; Lin, H.; Shih, H. *Appl. Phys. Lett.* **2003**, *83*, 3383.

(5) (a) Sathyanarayana, S. *J. Electrochem. Soc.* **1985**, *15*, 453. (b) Chen, J.; Bradhurst, D. H.; Dou, S. X.; Liu, H. K. *J. Electrochem. Soc.* **1999**, *146*, 3606.

(6) (a) Huang, L. S.; Yang, S. G.; Li, T.; Gu, B. X.; Du, Y. W.; Lu, Y. N.; Shi, S. Z. *J. Cryst. Growth* **2004**, *260*, 130. (b) Pan, Z. W.; Dai, Z. R.; Wang, Z. L. *Science* **2001**, *291*, 1947. (c) Huang, M.; Wu, Y.; Feick, H.; Tran, N.; Weber, E.; Yang, P. *Adv. Mater.* **2001**, *13*, 113. (d) Wang, Z. L.; Kong, X. Y.; Zuo, J. M. *Phys. Rev. Lett.* **2003**, *91*, 185502.

(7) (a) Kong, X. Y.; Wang, Z. L. *Nano Lett.* **2003**, *3*, 1625. (b) Lao, J. Y.; Huang, J. Y.; Wang, D. Z.; Ren, Z. F. *Nano Lett.* **2003**, *3*, 235. (c) Gao, P. X.; Wang, Z. L. *J. Am. Chem. Soc.* **2003**, *125*, 11299.

(8) (a) Zou, G.; Li, H.; Zhang, D.; Xiong, K.; Dong, C.; Qian, Y. *J. Phys. Chem. B* **2006**, *110*, 1632. (b) Liang, J.; Liu, J.; Xie, Q.; Bai, S.; Yu, W.; Qian, Y. *J. Phys. Chem. B* **2005**, *109*, 9463. (c) Liang, Z.; Zhu, Y.; Hu, X. *J. Phys. Chem. B* **2004**, *108*, 3488. (d) Li, F.; Ding, Y.; Gao, P.; Xin, X.; Wang, Z. L. *Angew. Chem., Int. Ed.* **2004**, *43*, 5238.

(9) (a) Liu, B.; Zeng, H. C. *J. Am. Chem. Soc.* **2004**, *126*, 8124. (b) Guo, L.; Ji, Y.; Xu, H.; Simon, P.; Wu, Z. *J. Am. Chem. Soc.* **2002**, *124*, 14864. (c) Shi, W.; Wang, C.; Wang, H.; Zhang, H. *Cryst. Growth Des.* **2006**, *6*, 915. (d) He, T.; Chen, D.; Jiao, X.; Xu, Y.; Gu, Y. *Langmuir* **2004**, *20*, 8404. (e) Cao, M.; Hu, C.; Wang, Y.; Guo, Y.; Guo, C.; Wang, E. *Chem. Commun.* **2003**, *15*, 1884.

(10) (a) Mo, M.; Yu, J. C.; Zhang, L.; Li, S. *Adv. Mater.* **2005**, *17*, 756. (b) Tian, Z. R.; Voigt, J. A.; Liu, J.; McKenzie, B.; McDermott, M. J. *J. Am. Chem. Soc.* **2002**, *124*, 12954. (c) He, T.; Chen, D.; Jiao, X.; Wang, Y. *Adv. Mater.* **2006**, *18*, 1078. (d) Liu, B.; Zeng, H. C. *J. Am. Chem. Soc.* **2004**, *126*, 16744. (e) Taubert, A.; Glasser, G.; Palms, D. *Langmuir* **2002**, *18*, 4488.

10.1021/cm070784g CCC: $40.75
Published on Web 12/22/2007

In a recent communication, we reported a facile method for the synthesis of mesoporous Co_3O_4 nanowire arrays from the hydrolysis of cobalt−ammonia complex ions.[13] In the reaction, an excess concentrated ammonia solution is added into an aqueous $Co(NO_3)_2$ solution to form $Co(NH_3)_6^{2+}$ complex ions. The homogeneous solution is then heated at 90 °C, which drives the evaporation of the dissolved ammonia and the hydrolysis of $Co(NH_3)_6^{2+}$. The resulting $Co(OH)_2$ is then oxidized and dehydrated into the final products.

In this report, we extend this ammonia-evaporation-induced synthetic method to other metal (Ni, Cu, Zn, and Cd) hydroxide/oxide materials and obtain a variety of interesting nanostructures, including hierarchical CuO spheres with radiating nanoplates, densely branched ZnO nanowires, $Cd(OH)_2$ nanofibers, and $Ni(OH)_2$ nanoplates. A subsequent thermal treatment can convert the hydroxides into oxides without a major morphological change.

Although ammonia has been commonly employed in many nanomaterial syntheses,[8,14] it generally needs to work together with other surfactants for structure directing. In our method, ammonia alone controls both the precipitation and the passivation of crystal surfaces. An interesting feature of this method is that the nanostructures grow in a dynamic environment with a continuous decrease of pH and ammonia concentration in the solution. The pH controls the charges carried by the particles while the ammonia molecules can passivate the surface and thereby influence the growth and aggregation behaviors of the particles. As a result, when the reaction starts with a high ammonia concentration and pH, the particles formed are stable in the solution. This is the "incubation" period that produces the primary particles. With the gradual decrease of the pH and ammonia concentration, the primary particles attach to each other and form the various hierarchical nanostructures. In addition to the synthesis and mechanism studies, we have also investigated the electrochemical reactivities of CuO spheres, CdO nanofibers, and NiO nanoplates with lithium and demonstrated their potential application as anode materials for lithium ion batteries.

Experimental Section

Chemicals. $Cu(NO_3)_2 \cdot 3H_2O$ (98.0–102.0%), $Zn(NO_3)_2 \cdot 6H_2O$ (98%), $Cd(NO_3)_2 \cdot 4H_2O$ (98%), $NiCl_2$ (99.3%), poly(vinylidene fluoride) (MW = 530 000), 1-methyl-2-pyrrolidinone (anhydrous, 99.5%), dimethyl carbonate (DMC, anhydrous, 99+%), ethylene carbonate (EC, anhydrous 99%), and $LiPF_6$ (99.99%) are from Sigma-Aldrich; concentrated ammonia solution (28–30 wt %) is from Mallinckrodt Chemicals. Acetylene carbon black and lithium foil (99.9%) is from Alfa Aesar; glass microfiber filter GF/D is from Whatman. Nanopure water (18.2 MΩ) has been used throughout our experiments.

Table 1. Experimental Details for the Synthesis of Hydroxide/Oxide Nanostructures

	inorganic salt concentrations	initial pH	annealing conditions for conversion to oxide
CuO	2.5–200 mM $Cu(NO_3)_2$	11.4	n/a
ZnO	20–200 mM $Zn(NO_3)_2$	10.4–11.8	n/a
$Cd(OH)_2$	20–80 mM $Cd(NO_3)_2$	>14	300 °C, 2h
$Ni(OH)_2$	10–80 mM $NiCl_2$	>14	300 °C, 2h

Synthetic Procedures. $Cu(NH_3)_4^{2+}$ and $Zn(NH_3)_4^{2+}$ complex cations were prepared by adding a concentrated ammonia solution dropwise into the corresponding metal salt aqueous solution until the pH reached the desired value under vigorous stirring (see Table 1 for synthetic details). $Cd(NH_3)_4^{2+}$ and $Ni(NH_3)_6^{2+}$ complex cations were prepared by directly dissolving $Cd(NO_3)_2$ and $NiCl_2$ in a concentrated ammonia solution. The resulting homogeneous solutions were then transferred to covered Petri dishes and gently heated in an oven at 90 °C overnight (about 14 h). Nanostructured CuO, ZnO, $Cd(OH)_2$, and $Ni(OH)_2$ were formed in the solution as either precipitates or floating films (for ZnO branched nanowires). For $Cd(OH)_2$ and $Ni(OH)_2$, a subsequent thermal treatment transforms the hydroxides into oxides. The reactions involved are shown below:[15]

$$M^{2+} + nNH_3 \rightarrow M(NH_3)_n^{2+} \quad (n = 4 \text{ for } Cu^{2+}, Cd^{2+}, Zn^{2+}; \; n = 6 \text{ for } Ni^{2+}) \quad (1)$$

$$M(NH_3)_n^{2+} + 2OH^- \xrightarrow{90\ ^\circ C} M(OH)_2 + nNH_3 \quad (2)$$

$$M(OH)_2 \rightarrow MO + H_2O \quad (3)$$

Characterization. Powder X-ray diffraction (XRD) patterns were obtained on a Riguka powder diffractometer operating at 40 kV and 25 mA, using Cu Kα radiation. Data were collected from 15° to 70° with a sampling interval of 0.01° per step and a counting rate of 1 s per step. Sample morphologies were examined in a Sirion scanning electron microscope operating at 15 kV and in a Tecnai TF-20 transmission electron microscope operating at 200 kV.

Lithium Ion Battery Measurements. The performances of the synthesized nanostructured metal oxides as anode materials in lithium ion batteries were examined in two-electrode test cells. The oxides were mixed with acetylene carbon black and poly(vinylidene fluoride) polymer binder with a mass ratio of 72:20:8. The mixture was first homogeneously dispersed in 1-methyl-2-pyrrolidinone to form a slurry and then vaccuum-dried at 110 °C for 2 h. The resulting mixture was used as the cathode; the anode is Li foil. A glass microfiber filter was used as the separator, which was infiltrated with 1 M $LiPF_6$ in 1:1 (w/w) EC and DMC electrolyte. These components were assembled in a Swagelok cell in the glovebox filled with a highly pure Ar gas. Cycling tests were performed from 3.0 to 0.01 V at the rate of 111 mA/g using a Maccor 4304 battery test system.

Results and Discussion

1: CuO. For the synthesis of CuO nanostructures, we maintained the pH of the starting solution at 11.4 and varied the initial concentration of $Cu(NO_3)_2$ from 2.5 to 200 mM.

(11) (a) Martin, C. R. *Science* **1994**, *266*, 1961. (b) Wu, G. S.; Xie, T.; Yuan, X. Y.; Li, Y.; Yang, L.; Xiao, Y. H.; Zhang, L. D. *Solid State Commun.* **2005**, *134*, 485. (c) Matsui, K.; Kyotani, T.; Tomita, A. *Adv. Mater.* **2002**, *14*, 1216.
(12) Nam, K. T.; Kim, D.; Yoo, P. J.; Chiang, C.; Meethong, N.; Hammond, P. T.; Chiang, Y.; Belcher, A. M. *Science* **2006**, *312*, 885.
(13) Li, Y.; Tan, B.; Wu, Y. *J. Am. Chem. Soc.* **2006**, *128*, 14258.
(14) (a) Tak, Y.; Yong, K. *J. Phys. Chem. B* **2005**, *109*, 19263. (b) Xu, C. X.; Wei, A.; Sun, X. W.; Dong, Z. L. *J. Phys. D: Appl. Phys.* **2006**, *39*, 1690. (c) Lu, C.; Qi, L.; Yang, J.; Zhang, D.; Wu, N.; Ma, J. *J. Phys. Chem. B* **2004**, *108*, 17825. (d) Collins, A.; Carriazo, D.; Davis, S. A.; Mann, S. *Chem. Commun.* **2004**, 568.
(15) Cotton, F. A.; Wilkinson, G. *Advanced Inorganic Chemistry*; Wiley & Sons: New York, 1999.

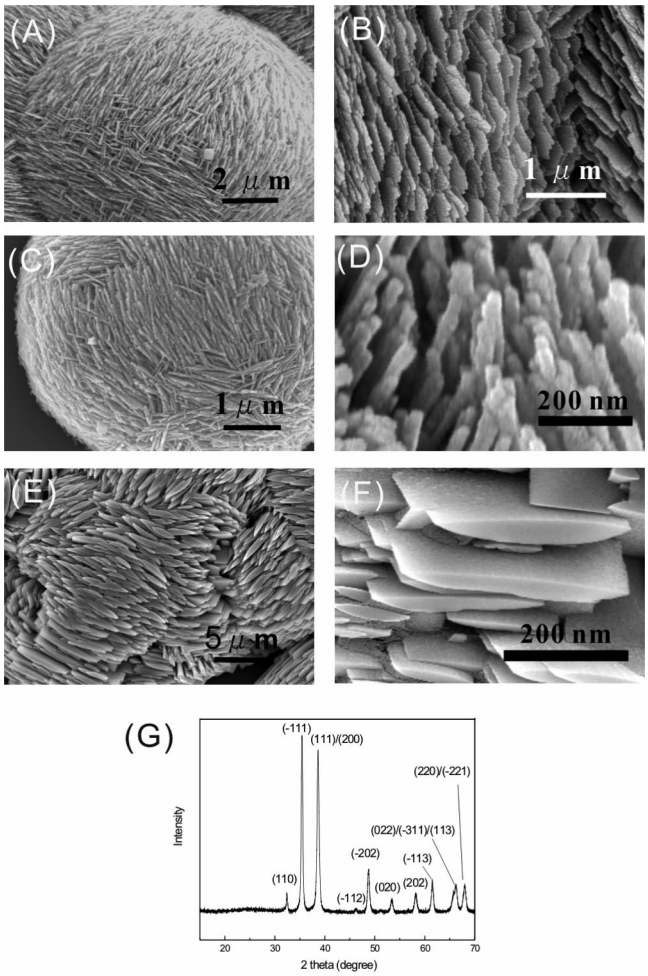

Figure 1. SEM images of CuO nanostructures synthesized with (A, B) 20 mM, (C, D) 10 mM, and (E, F) 100 mM $Cu(NO_3)_2$. The initial solution pH is adjusted to 11.4 with ammonia for all samples. (G) is a typical XRD pattern.

Different morphologies were observed. When the initial concentration of $Cu(NO_3)_2$ is 20 mM, the products have spherical bodies with radiating nanoplates (Figure 1A,B). Their thickness is <100 nm. Locally these nanoplates are arranged parallel to each other, resembling the nacreous structure.[10b,16] On a sphere, domains with various nanoplate alignments coexist. When we reduce the initial concentration of $Cu(NO_3)_2$ to 10 mM, the CuO products still maintain the spherical shape. However, the building blocks change to nanorods. If the concentration is further decreased to 2.5 mM, the spheres are made up of coalesced particles. We have also increased the initial concentration of $Cu(NO_3)_2$ to 100 mM. Although the building blocks are still plates, they present a different shape whose thickness is greatest at the center and tapers off to the two sides (Figure 1E,F). Further increasing the concentration to 200 mM shows the same result as that at 100 mM. All these samples have been characterized by XRD, showing that they are made of monoclinic CuO (Figure 1G).

Transmission electron microscopy (TEM) characterization was also conducted to understand the crystallinity and the crystalline orientation of these building blocks. Samples were prepared by breaking down the spheres via sonication. Figure 2A shows a TEM image of the nanoplate synthesized with an initial $Cu(NO_3)_2$ concentration of 20 mM. The nanoplate has a diamond shape with rough and fuzzy edges. On the basis of the selected area electron diffraction (SAED) pattern, it can be determined that the diamond long axis is along the [010] direction and the short axis is along the [100] direction, consistent with other reported results.[8a,9a,17] It is noteworthy that each diffraction spot spreads slightly into an arc, indicating that these nanoplates are not perfectly single-crystalline. High-magnification TEM images shows that they are made up of attached nanoparticles of ~10 nm in size. All of the above information suggests that the oriented attachment of the primary nanoparticles governs the nanoplate growth.[9a,17b] For the nanowire building blocks obtained with 10 mM $Cu(NO_3)_2$, TEM analysis shows that they have similar rough edges and that their growth is along the [010] direction (Figure 2C), also consistent with previous reports about monoclinic CuO nanowires.[14c,17a] To our surprise, the thick plates obtained with 100 mM $Cu(NO_3)_2$, however, have completely different surface features and an unconventional crystallographic orientation (Figure 2D,E). Their surfaces are very smooth, and both the contrast and well-defined edge clearly indicate their single-crystalline nature, as confirmed by the sharp diffraction spots in the SAED pattern. Moreover, the zone axis of the SAED pattern is indexed to be [010] and not [001]. That means that these plates are grown along the $a-c$ plane of monoclinic CuO, which, to our best knowledge, has not been reported before.

To understand the growth mechanism, an analysis of the reaction process becomes necessary. The reaction solution initially contains $Cu(NH_3)_4^{2+}$ with excess dissolved ammonia. With the evaporation of ammonia when heated in the oven, the hydrolysis of the $Cu(NH_3)_4^{2+}$ complex occurs, forming $Cu(OH)_2$, which then dehydrates to CuO primary nanoparticles. We measured the decrease of the solution pH with reaction time, which reflects the decrease of the ammonia concentration during the reaction process (see Supporting Information Figure SI-1). The surface of the CuO nanoparticles may be capped by the ammonia or anions such as NO_3^- in the solution. However, we have tried to use $CuCl_2$, $CuSO_4$, or $CuAc_2$ instead of $Cu(NO_3)_2$ or to add additional $NaNO_3$, as much as 200 mM, while keeping the Cu^{2+} concentration the same. No change of products has been observed. Therefore, we conclude that the surface passivation of ammonia plays the major role in controlling the structures of the products.

There are the following two major chemical equilibria during hydrolysis:

$$Cu(NH_3)_4^{2+}(aq) + 2OH^-(aq) \leftrightarrow Cu(OH)_2(s) + 4NH_3(aq)\ K_1$$

$$NH_3(aq) + H_2O(l) \leftrightarrow NH_4^+(aq) + OH^-(aq)\ \ K_b$$

One can then derive that when the hydrolysis starts, $[NH_3]/[Cu(NH_3)_4^{2+}] = K \cdot [Cu(NH_3)_4^{2+}]^{-2/3}$, in which $K = (K_1K_b)^{1/3}$. The $[NH_3]/[Cu(NH_3)_4^{2+}]$ ratio indicates the concentration of ammonia available in the solution to passivate the surface of the CuO nanoparticles. Considering the four reaction

(16) (a) Addadi, L.; Joester, D.; Nudelman, F.; Weiner, S. *Chem. Eur. J.* **2006**, *12*, 980. (b) Halloran, J. *Science* **2006**, *311*, 479.

(17) (a) Chang, Y.; Zeng, H. C. *Cryst. Growth Des.* **2004**, *4*, 397. (b) Zhang, Z.; Sun, H.; Shao, X.; Li, D.; Yu, H.; Han, M. *Adv. Mater.* **2005**, *17*, 42. (c) Liu, J.; Huang, X.; Li, Y.; Sulieman, K. M.; He, X.; Sun, F. *Cryst. Growth Des.* **2006**, *6*, 1690.

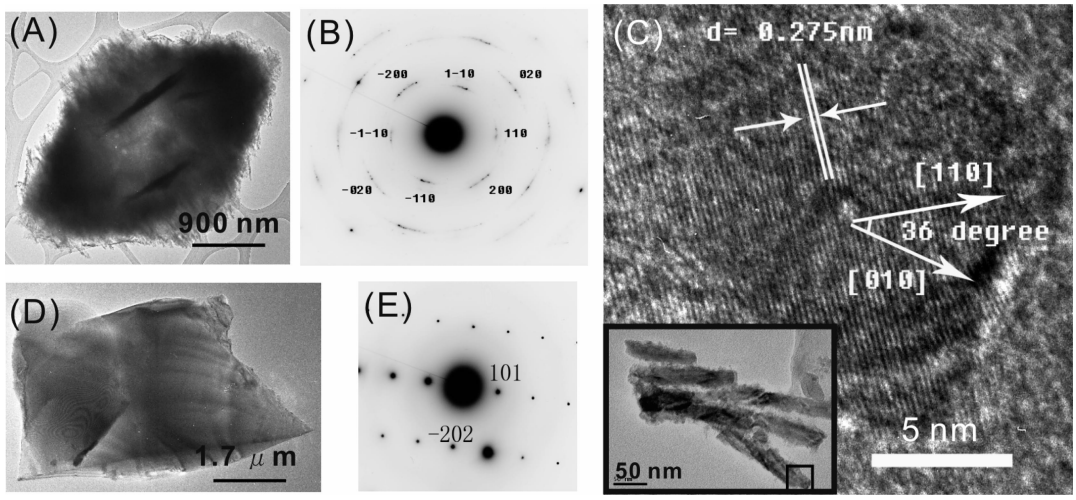

Figure 2. TEM characterization of the CuO building blocks synthesized at different $Cu(NO_3)_2$ concentrations. (A, B) nanoplate synthesized with 20 mM $Cu(NO_3)_2$; (C) nanowire synthesized with 10 mM $Cu(NO_3)_2$ (the inset shows the overview of the nanowires with the enclosed end magnified); (D, E) thick plate synthesized with 100 mM $Cu(NO_3)_2$.

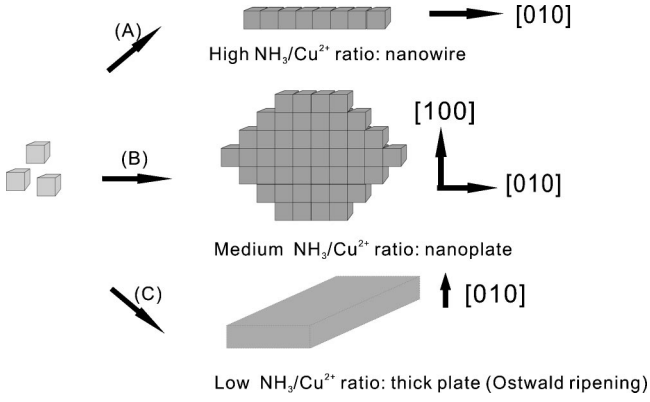

Figure 3. Growth mechanism of CuO at various NH_3/Cu^{2+} ratios. (A) Oriented attachments of CuO primary nanocrystals along the [010] direction to form nanowires at a high NH_3/Cu^{2+} ratio; (B) oriented attachments along the [010] and [100] directions to form nanoplates at a medium NH_3/Cu^{2+} ratio; (C) Ostwald ripening of the CuO primary nanoparticles to form thick nanoplates at a low NH_3/Cu^{2+} ratio.

solutions used in the synthesis (with different concentrations of 2.5, 10, 20, and 100 mM, respectively), the reaction solution with the lowest initial $Cu(NO_3)_2$ concentration has the highest $[NH_3]/[Cu(NH_3)_4^{2+}]$ ratio. This has been quantitatively confirmed in our experiments.

When ammonia molecules passivate the CuO surface, they form coordinate bonds with the Cu ions on the surface. The density of the adsorbed ammonia depends on the density of the Cu^{2+} ions on the crystal plane, as suggested by a previous report.[17b] Calculations based on a monoclinic CuO unit cell show that the Cu^{2+} ion densities are 12.5 ions nm^{-2}, 8.5 ions nm^{-2}, and 11.5 ions nm^{-2} for the (001), (010), and (100) planes, respectively.[17b] Therefore, it is reasonable to expect that ammonia has the highest affinity with the (001) plane, followed by the (100) plane, and then the (010) plane.

Combining the above information, we can come up with a qualitative explanation (Figure 3). When the initial $Cu(NO_3)_2$ concentration is only 2.5 mM, NH_3 is in great excess (NH_3/Cu^{2+} is measured to be >14 when the hydrolysis starts). As a result, all the primary CuO nanocrystal planes are densely passivated, resulting in a weak driving force for further aggregation into nanowires or nanoplates. Increasing the concentration to 10 mM can lead to a less dense passivation on the (010) plane because the (010) plane has the lowest affinity with NH_3, while the passivation layers on the (100) and (001) planes remain largely intact. Therefore, oriented attachment along the *b* axis occurs to form nanowires. Further increasing the concentration to 20 mM results in the significant depassivation on the (100) plane as well. Consequently, oriented attachment along both the *a* and the *b* axes becomes possible. This explains the observed diamond CuO nanoplates with dimensional sizes along the different axes in the order $b > a > c$.

However, things are different when the $Cu(NO_3)_2$ concentration is as high as 100 mM. From the single-crystalline nature of the thick plate and its smooth surface, we suggest that Ostwald ripening is the major growth mechanism. At such a high $Cu(NO_3)_2$ concentration, there is not enough ammonia to effectively passivate the crystal surfaces when the hydrolysis starts ($NH_3/Cu^{2+} < 2$). The crystal growth is then determined by the relative intrinsic surface energy. The relative surface energies of the bare (001), (010), and (100) planes have just the opposite trend than those of the passivated surfaces: the bare (010) plane has the lowest surface energy because it has the lowest surface charge density while the bare (100) and (001) planes have the higher surface energies. Therefore, when the nucleus grows through the Ostwald ripening mechanism, the growth rates along *a*- and *c*-axes are higher than that along the *b*-axis, resulting in the formation of a plate with the *b*-axis as the shortest dimension.

Our mechanism is consistent with some previous reports.[17b,c,18] In the investigations of the oriented attachment of anatase TiO_2 nanoparticles, Penn and Banfield[19] observed that the attachment occurs on the {112} or {001} planes for bare nanoparticles, while Adachi and co-workers[18] observed that the attachment occurs on the {101} planes for surfactant-capped nanoparticles. This is because the surface density of

(18) Adachi, M.; Murata, Y.; Takao, J.; Jiu, J.; Sakamoto, M.; Wang, F. *J. Am. Chem. Soc.* **2004**, *126*, 14943.
(19) (a) Penn, R. L.; Banfield, J. F. *Geochim. Cosmochim. Acta* **1999**, *63*, 1549. (b) Penn, R. L.; Banfield, J. F. *Science* **1998**, *281*, 969.

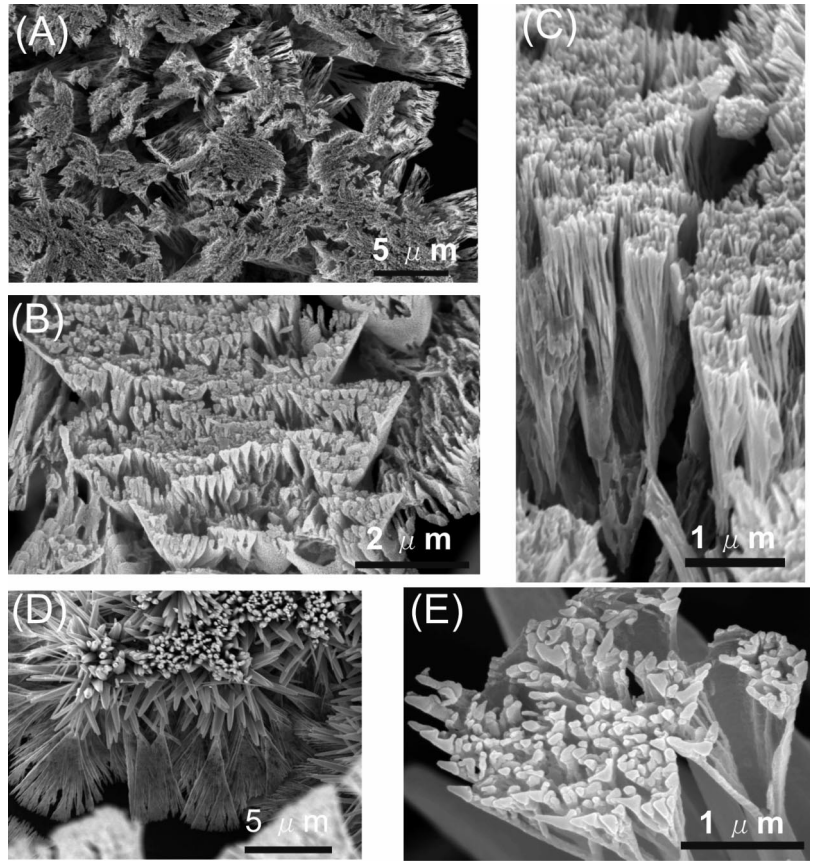

Figure 4. SEM images of the ZnO branching structures on the top side and the edges of the floating film.

the Ti atoms with the hydroxyl of the {001} surface is higher than that on the {101} planes. As a result, more surfactant molecules are adsorbed on the {001} planes, which hinder the attachment on the {001} planes. In another investigation, Zhang and co-workers[17b] reported the three-dimensional aggregation of CuO primary nanoparticles into monocrystalline architectures. They suggested that the surface density of the Cu^{2+} ions on a crystal plane determines the density of the adsorbed formamide molecules. The different Cu^{2+} ion density on the (100), (010), and (001) planes leads to the anisotropic aggregation of primary nanoparticles.

2: ZnO. When we applied the same method to ZnO, we observed the formation of white precipitates at the bottom of the Petri dish. Scanning electron microscopy (SEM) characterization shows that the precipitates have the morphology of a flower with radiating nanowires (see Supporting Information Figure SI-2A,B). In addition, we have also observed a floating white film on the surface of the reaction solution. On the down side of the film that faces the solution are found arrays of ZnO nanowires (see Supporting Information Figure SI-2C,D) while on the top side and around the edges are found densely branched ZnO nanostructures as shown in Figure 4. They have cone-like shapes formed by the aligned thin nanowires on the top (Figure 4A−C) with fan-blade shaped planar edges (Figure 4D). In regions without the extensive growth of the branched structures, we can observe that the branches grow out of the hollow nanotubes (Figure 4E). XRD analysis shows that all the products are made of crystalline ZnO with a wurtzite structure (see Supporting Information Figure SI-3).

Their detailed texture and crystal orientation were further investigated by TEM. Figure 5A shows the overview of a broken piece at low magnification. It has a roughly triangle shape with individual nanowires protruding out from the end. The regions enclosed by the rectangles “b” and “c” are magnified in Figure 5B,C, which clearly shows that the structure is made of densely packed nanowires with diameters ranging from 20 to 40 nm. The SAED pattern of the whole piece gives a diffraction pattern close to that of a single crystal with the zone axis along the [011] direction of the wurtzite ZnO, although the whole structure is made from numerous nanowires, and proves that all the nanowires are highly crystalline and well aligned. A fine examination of the individual nanowires shows that their surface is rough and covered with nanoparticles of about 5 nm in size. This feature again suggests the oriented attachment as the possible mechanism of the nanowire growth and will be further discussed later. Structure crystallinity is also confirmed by high resolution TEM (HRTEM) image shown in Figure 5G,H. The *d* spacing between the adjacent lattice planes is 2.82 Å in Figure 5G and 2.48 Å in Figure 5H, corresponding to the distance between two (100) and $(0\bar{1}1)$ crystal planes, respectively. Surprisingly, none of the nanowires that we have examined grow along the [001] direction as observed in most of the previous works on ZnO nanowires. In Figure 5H, profiles of attached nanoparticles are easily identifiable. Some of them show the same lattice orientation and merge into a nanowire while others do not, probably still in the process of self-adjustment for oriented attachment.

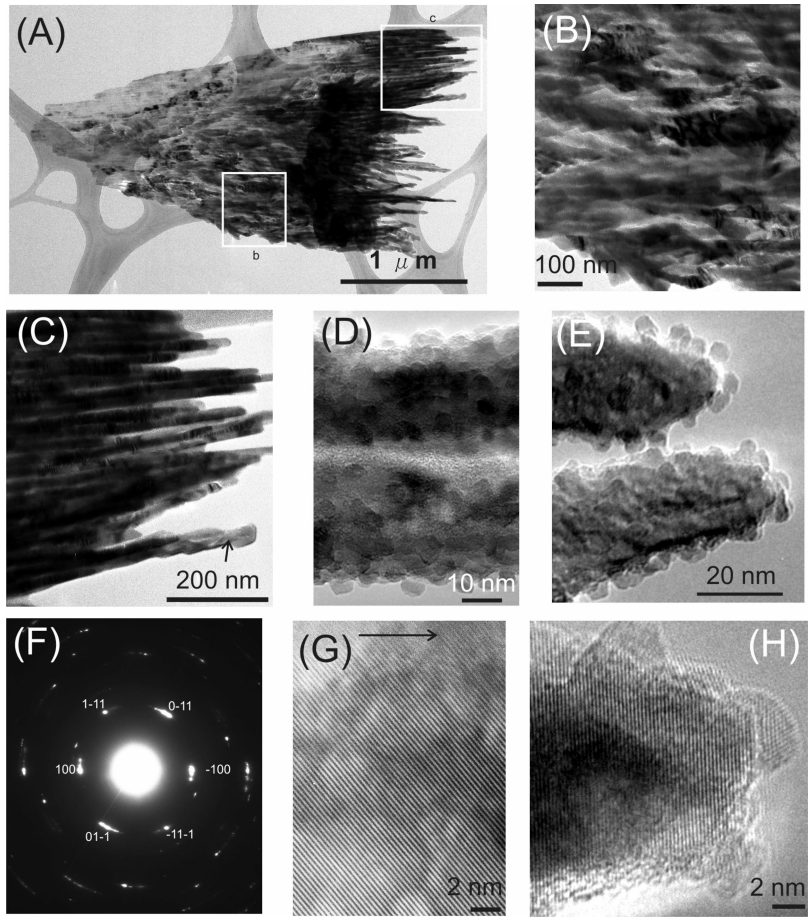

Figure 5. TEM images of ZnO branching structures. (A) An overall view of a broken piece of the branching structure. The two regions enclosed by the rectangles are magnified in B and C, respectively. D and E show the rough surface of the nanowires covered with ZnO nanoparticles of about 5 nm in size. (F) SAED pattern indexed along the [011] zone axis. G and H are HRTEM images of the constituent nanowires recorded at different regions. The arrow in G indicates the direction of the nanowire long axis. The *d* spacing between adjacent lattice planes is 2.82 Å in G and 2.48 Å in H, corresponding to the distance between two (100) and (0$\bar{1}$1) crystal planes, respectively.

The formation of the branched structure has been recognized for decades in many out-of-equilibrium processes such as, for example, the crystallization of snowflakes, the electrodeposition of metals at high voltage, and the formation of mineral dendrites.[20] In the diffusion-limited aggregation (DLA) model, the irreversible aggregation of randomly moving particles results in the self-amplifying growth of bulges and the formation of fractal patterns. Incorporation of surface tension and structural anisotropy can further model the formation of the dense branching and dendritic patterns.

The TEM characterization shows that small ZnO nanoparticles are attached to the surface of the nanowires in the densely branched nanostructures. This suggests that the attachment of primary nanoparticles could be the growth mechanism. We have also investigated the morphology evolution of the floating film at the different reaction stages and observed that the growth of branches was initiated after the reaction had progressed for 7 h (see Supporting Information Figure SI-4). At this time, the solution pH was measured to be 8.7, which is close to the "point of zero charge" (PZC) for ZnO.[20,21]

Taking into account these observations, we suggest the following process for the formation of the branched nanostructures: the initial stage is the formation of the primary ZnO nanoparticles as a result of the hydrolysis of $Zn(NH_3)_4^{2+}$ complex ions and subsequent dehydration. At this stage, the concentration of ammonia is high and the pH is higher than the PZC of ZnO. The surface passivation by ammonia and the similar negative charge carried by the primary nanoparticles result in a weak driving force for nanoparticle aggregation. Dispersible ZnO primary nanoparticles can be separated and observed in TEM at this stage of the reaction. Further evaporation of ammonia will reduce the surface passivation and the pH of the solution. When the pH gets close to the PZC, the nanoparticles quickly aggregate and form the densely branched nanostructures. Because the escape of ammonia from the solution occurs at the solution surface, the region close to the surface will reach a pH of the PZC earlier than in other regions of the solution. This can explain why the densely branched nanostructures form at the surface of the solution. A similar mechanism based on the oriented

(20) Ben-Jacob, E.; Garik, P. *Nature* **1990**, *343*, 523.
(21) Blok, L.; De Bruyn, P. L. *J. Colloid Interface Sci.* **1970**, *32*, 518.
(22) (a) Lu, L.; Kobayashi, A.; Kikkawa, Y.; Tawa, K.; Ozaki, Y. *J. Phys. Chem. B* **2006**, *110*, 25013. (b) Wen, X.; Xie, Y.; Mak, M. W. C.; Cheung, K. Y.; Li, X.; Renneberg, R.; Yang, S. *Langmuir* **2006**, *22*, 4836.

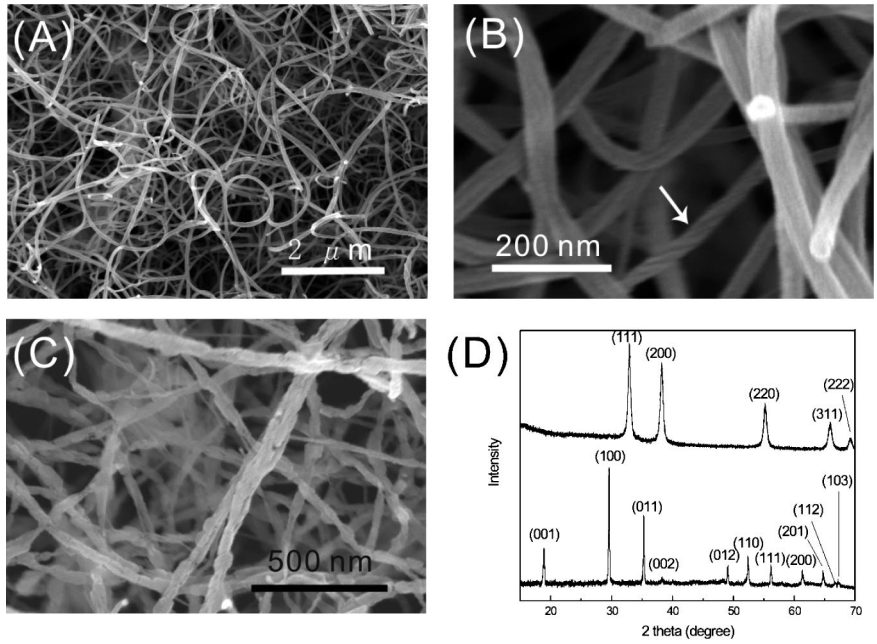

Figure 6. SEM images of (A, B) $Cd(OH)_2$ nanofibers synthesized with 1 mmol of $Cd(NO_3)_2$ in 50 mL of concentrated ammonia. (B) The white arrow marks a helical nanofiber, (C) CdO nanofibers after thermal treatment, and (D) XRD patterns of hexagonal β-$Cd(OH)_2$ (bottom) and cubic CdO (top) after annealing at 300 °C for 2 h.

attachments of primary nanoparticles has been recently proposed by Lu et al.[22a] and Wen et al.[22b] to explain dendritic silver nanostructures.

3: $Cd(OH)_2$ and CdO Nanofibers. Hydrolysis of $Cd(NH_3)_4^{2+}$ complex ions results in the formation of $Cd(OH)_2$ nanofibers (Figure 6). Their diameters vary from 30 to 70 nm, and their lengths are more than 10 μm. A closer view reveals that these nanofibers are composed of much thinner nanostrands, which intertwine with each other into bundles. Some of them form helical structure as indicated by the arrow in Figure 6B. Their crystallinity is confirmed by the XRD pattern (Figure 6D bottom pattern), and all the peaks of our final product can be assigned to the hexagonal β-$Cd(OH)_2$. These nanofibers were also examined with TEM (Figure 7). Some free single nanostrands with diameters of ~2 nm were observed as indicated by the arrow in Figure 7A. However, the $Cd(OH)_2$ nanofibers were unstable under electron beam irradiation. We could not obtain the detailed structural information of the nanofibers and their constituent nanostrands.

$Cd(OH)_2$ nanostrands with a diameter of 1.9 nm have been previously reported by Ichinose and co-workers.[23] The nanostrands were synthesized by raising the pH of a diluted $Cd(NO_3)_2$ solution, which induced the hydrolysis and the condensation of hydrated cadmium ions. The authors found that the nanostrand surface was positively charged and nanostrands could assemble into bundles with the assistance of a negatively charged dye or DNA molecules. However, only single nanostrands were formed in the absence of these molecules. In our synthesis, the formation of the nanofibers should follow a similar mechanism, that is, the hydrolysis of the $Cd(NH_3)_4^{2+}$ complex ions due to the evaporation of ammonia. The difference is that the nanofibers in our synthesis are bundles of nanostrands. This may be caused by the different pH values when the $Cd(OH)_2$ nanostrands form. In Ichinose's synthesis, the pH is below the PZC of $Cd(OH)_2$; the electrostatic repulsion between the positively charged nanostrands prevent them from forming the bundles. In our synthesis, the solution initially is very basic (pH > 14). With the evaporation of ammonia, the pH gradually becomes close to the PZC of $Cd(OH)_2$

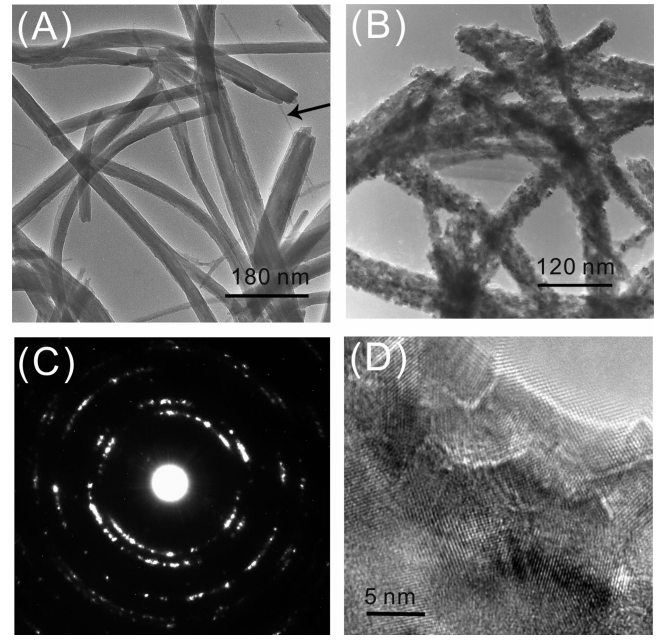

Figure 7. (A) TEM images of $Cd(OH)_2$ nanofibers, the black arrow marks a single nanostrand, (B) CdO nanofibers after thermal treatment and (C) its corresponding SAED pattern, indicating that the nanofibers are polycrystalline, and (D) HRTEM image of CdO nanofibers showing that they are made of nanocrystals.

(23) (a) Luo, Y.; Huang, J.; Ichinose, I. *J. Am. Chem. Soc.* **2005**, *127*, 8296. (b) Ichinose, I.; Huang, J.; Luo, Y. *Nano Lett.* **2005**, *5*, 97. (c) Ichinose, I.; Kurashima, K.; Kunitake, T. *J. Am. Chem. Soc.* **2004**, *126*, 7162.

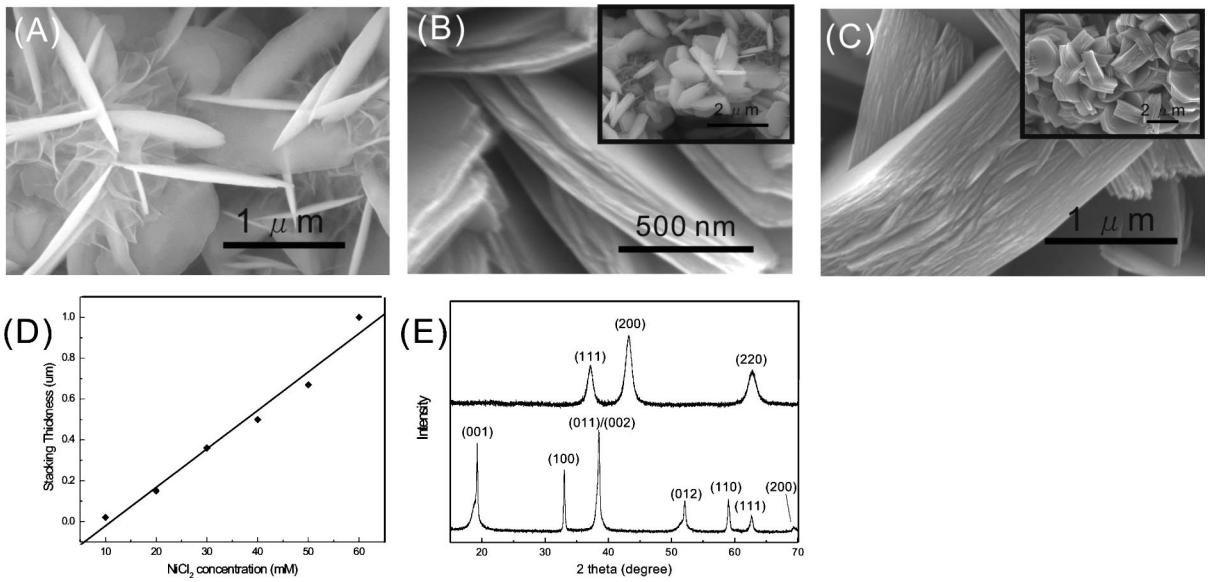

Figure 8. Characterization of nanoplates. (A−C) SEM images of $Ni(OH)_2$ nanoplates synthesized with different $NiCl_2$ concentrations (A) 10 mM, (B) 20 mM, and (C) 60 mM; (D) the linear dependence of the average nanoplate thickness on the $NiCl_2$ concentration; (E) XRD patterns of hexagonal β-$Ni(OH)_2$ (bottom pattern) and cubic NiO (top) formed by heating $Ni(OH)_2$ nanoplates at 300 °C for 2 h. Insets in B and C show the corresponding large area views of the samples.

(∼12–13).[24] Without the electrostatic repulsion between them, the nanostrands can spontaneously assemble into nanofibers.

$Cd(OH)_2$ nanofibers can be converted into CdO through a thermal treatment at 300 °C for 2 h. The XRD characterization shows only CdO peaks with the peaks broadened (Figure 6D top spectrum). SEM (Figure 6C) and TEM (Figure 7B) characterizations show that although the fibrous morphology is preserved, the CdO nanofibers have lost the nanostrand characteristic. The SAED pattern of an individual CdO nanofiber (Figure 7C) and the HRTEM image (Figure 7D) show that the nanofiber is polycrystalline.

4: $Ni(OH)_2$ and NiO Nanoplates. Hydrolysis of $Ni(NH_3)_6^{2+}$ complex ions results in the formation of $Ni(OH)_2$ nanoplates. Figure 8 shows the SEM images of the nanoplates synthesized with different initial $NiCl_2$ concentrations. Their thickness and shape depend on the $NiCl_2$ concentrations: lower concentration results in thinner nanoplates. At 10 mM, the formed nanoplates have a thickness of tens of nanometers and exhibit a circular outline. When the $NiCl_2$ concentration is increased to 20 mM, the nanoplates become hexagonal with an average thickness of ∼200 nm (Figure 8B). A detailed examination shows that they are made up of stacked thin nanoplates. At a concentration of 60 mM, the thickness further increases to ∼1 μm with more stacked thin nanoplates (Figure 8C). A plot of the average thickness versus the initial $NiCl_2$ concentrations shows a linear dependence (Figure 8D). This can be rationalized considering that the increased $NiCl_2$ concentration would result in more thin nanoplates for stacking. XRD characterization shows that the nanoplates are made of hexagonal β-$Ni(OH)_2$. TEM characterization shows that the nanoplates are single-crystalline with the *c*-axis perpendicular to the base plane (Figure 9A−C).

A thermal treatment at 300 °C for 2 h can completely transform $Ni(OH)_2$ nanoplates to NiO nanoplates with no observable morphological change (see Supporting Information Figure SI-5). The SAED pattern shows that the NiO nanoplates are also single-crystalline with the [111] axis perpendicular to the base plane (Figure 9E). Interestingly, besides the $\{2\bar{2}0\}$ and $\{4\bar{2}\bar{2}\}$ diffraction spots, some normally forbidden diffraction spots, such as 1/3{422} and 2/3{422}, also appear even though they are weak. This phenomenon has been previously recognized only for Ag and Au atomically flat nanoplates due to the multiply parallel twins on the {111} planes leading to a local hexagonal-like structure.[25] Here we are not very certain of their origin; it is probably caused by the thermal conversion which may give rise to "twin-like" in-plane defects. The single-crystalline nature of the NiO nanoplates can be understood as a result of the topotactic conversion from $Ni(OH)_2$ to NiO with a relationship of $Ni(OH)_2$ [001] || NiO [111] because cubic NiO consists of a similar stacking of Ni^{2+} and O^{2+} layers along the [111] direction as does $Ni(OH)_2$ along the [001] direction and the *d* space of the $Ni(OH)_2$ (002) planes matches that of the NiO (111) planes (compare the two XRD spectra in Figure 8E).

5: Battery Measurements. Since their discovery in 2000, transition metal oxides have become an important category of anode materials for lithium ion batteries.[2a] Their operations are based on the conversion mechanism, which involves the formation of metal nanograins dispersed in the Li_2O matrix during discharge, and the reoxidization of the metal nanograins to oxides when charged back, as shown by the reversible reaction $MO + 2Li^+ + 2e^- \leftrightarrow Li_2O + M$. Their large capacity and good cycleability outperform many traditional electrode materials. Nanostructured transition metal oxides have the advantages of a reduced Li^+ diffusion length and a high electrochemical reactivity associated with the small dimension, resulting in improved capacity and rate

(24) Borah, D.; Senapati, K. *Fuel* **2006**, *85*, 1929.

(25) (a) Cherns, D. *Philos. Mag.* **1974**, *30*, 549. (b) Kirkland, A. I.; Jefferson, D. A.; Duff, D. G.; Edwards, P. P. *Inst. Phys. Conf. Ser.* **1990**, *98*, 375. (c) Jin, R.; Cao, Y.; Mirkin, C. A.; Kelly, K. L.; Schatz, G. C.; Zheng, J. G. *Science* **2001**, *294*, 1901.

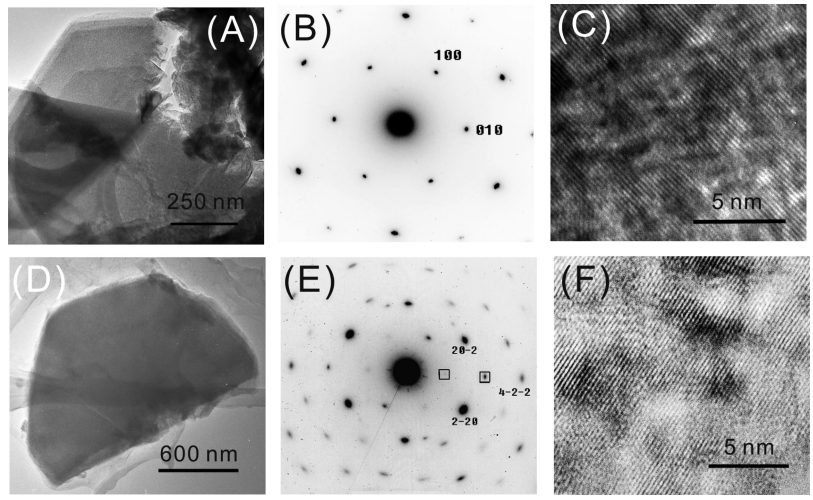

Figure 9. TEM images of (A) the overview of the $Ni(OH)_2$ nanoplate with its (B) corresponding SAED pattern indexed along the [001] zone axis and (C) HRTEM image showing the lattice fringes of the (100) planes; (D) the overview of the NiO nanoplate after thermal treatment with its (E) corresponding SAED indexed along [111] zone axis (the enclosed spots are formally forbidden diffraction spots $1/3(4\bar{2}\bar{2})$ and $2/3(4\bar{2}\bar{2})$); and (F) HRTEM image of NiO nanoplate showing the lattice fringes of the (110) planes.

capability.[2a,12,26] Here, we have investigated the electrochemical reactivity of the CuO, CdO, and NiO nanostructures that we have synthesized.

Before the pioneering work by Poizot et al.,[2a] Li−CuO primary cells had been produced on an industrial scale in 1980s. Many discharge reaction mechanisms had been proposed.[27] Tarascon and co-workers[28a,b] recently have verified that CuO is reduced to Cu nanograins during discharge through an intermediate Cu_2O phase by comprehensive in situ XRD and electron diffraction studies. In their investigation, CuO has a capacity around 400 mA h/g depending on the particle size. Similar capacity results have been demonstrated by some other research groups.[28c]

In our investigation, the CuO sample is made of spheres with radiating nanoplates as shown in Figure 1A. Its discharge curve exhibits two processes: a gradual slope in the range of 1.2−0.7 V for a 2.2 Li uptake, followed by a drastic drop below 0.7 V for a 0.15 Li uptake (Figure 10A). The first process corresponds to the continuous reduction from the Cu(II) species to Cu(I) and finally to Cu(0), and the second process corresponds to the catalytic decomposition of liquid electrolyte to form a solid electrolyte interphase (SEI) at such a low voltage.[28a] The total capacity of our CuO sample is about 800 mA h/g in the first discharge. However, the following charge capacity is very small, <250 mA h/g. Despite the contribution from the SEI layer formation, such a large difference in capacity indicates that the reaction is rather irreversible. Theoretically, the capacity value of CuO is 674 mA h/g assuming a reversible stoichiometric 2e transfer; however, Tarascon suggested that the reduced metallic Cu mainly reoxidizes to Cu_2O and not to CuO during charge[28a,b] therefore having a reduced theoretic capacity of only 375 mA h/g. Indeed, reoxidization to Cu_2O is more energetically favored because the very similar crystal structures of Li_2O and Cu_2O facilitate the ion-exchange-like replacement of Li^+ with Cu^+ in the O^{2-} lattice. It is also interesting to notice that the charge−discharge capacities of our CuO sample increase gradually at the first several cycles, especially for the charge capacity, and reach the maxima at the fifth or sixth cycle to give a capacity value of 420 mA h/g for discharge and of 360 mA h/g for charge (Figure 10D). We believe that this is a result of the gradual degradation of the compact structure of the CuO spheres, which exposes the initially inaccessible core to the electrochemical reaction. The structure degradation of the CuO spheres can be verified by the SEM image of our electrode material after 5 cycles (see Supporting Information Figure SI-5). After 20 cycles, the capacities decay to 250 mA h/g.

To our best knowledge, CdO has not previously been tested as an anode material, presumably because of the general concerns about its toxicity and low theoretical value (417 mA h/g). In our investigation, the calcined CdO nanofibers show a decent initial discharge capacity of 570 mA h/g. However, their cycleability is poor, and the charge/discharge capacities quickly drop to and finally stabilize at only 70 mA h/g after 10 cycles (Figure 10 B,E).

A NiO-based anode has also been examined recently and demonstrates a capacity from 200 to 400 mA h/g.[2a,29] However, capacity decay is a very severe problem for all of them. Here we investigated the electrochemical reactivity of our calcined NiO nanoplates. Figure 10C shows the charge/discharge curves of the first two cycles. It exhibits a well-defined plateau on the first discharge at around 0.6 V for a 2.4 Li uptake during the first cycle, followed by a slope down to 0 V for a 0.67 Li uptake. The first discharge capacity is 1100 mA h/g; however, only 650 mA h/g can be recovered. In the second and following discharge, the plateau becomes

(26) Aricò, A. S.; Bruce, P.; Scrosati, B.; Tarascon, J.; van Schalkwijk, W. *Nat. Mater.* **2005**, *4*, 366.
(27) (a) Ikeda, H.; Narukawa, S. *J. Power Sources* **1983**, *9*, 329. (b) Bates, R. ; Jumel, Y. *Lithium Batteries*; Academic Press: New York, 1983. (c) Novak, P. *Electrochim. Acta* **1985**, *30*, 1687.
(28) (a) Grugeon, S.; Laruelle, S.; Herrera-Urbina, R.; Dupont, L. P.; Tarascon, J. M. *J. Electrochem. Soc.* **2001**, *148*, A285. (b) Débart, A.; Dupont, L.; Poizot, P.; Leriche, J. B.; Tarascon, J. M. *J. Electrochem. Soc.* **2001**, *148*, A1266. (c) Morales, J.; Sánchez, L.; Martín, F.; Ramos-Barrado, J. R.; Sánchez, M. *Electrochim. Acta* **2004**, *49*, 4589.
(29) (a) Needham, S. A.; Wang, G. X.; Liu, H. K. *J. Power Sources* **2006**, *159*, 254. (b) Yuan, L.; Guo, Z. P.; Konstantinov, K.; Munroe, P.; Liu, H. K. *Electrochem. Solid-State Lett.* **2006**, *9*, A524.

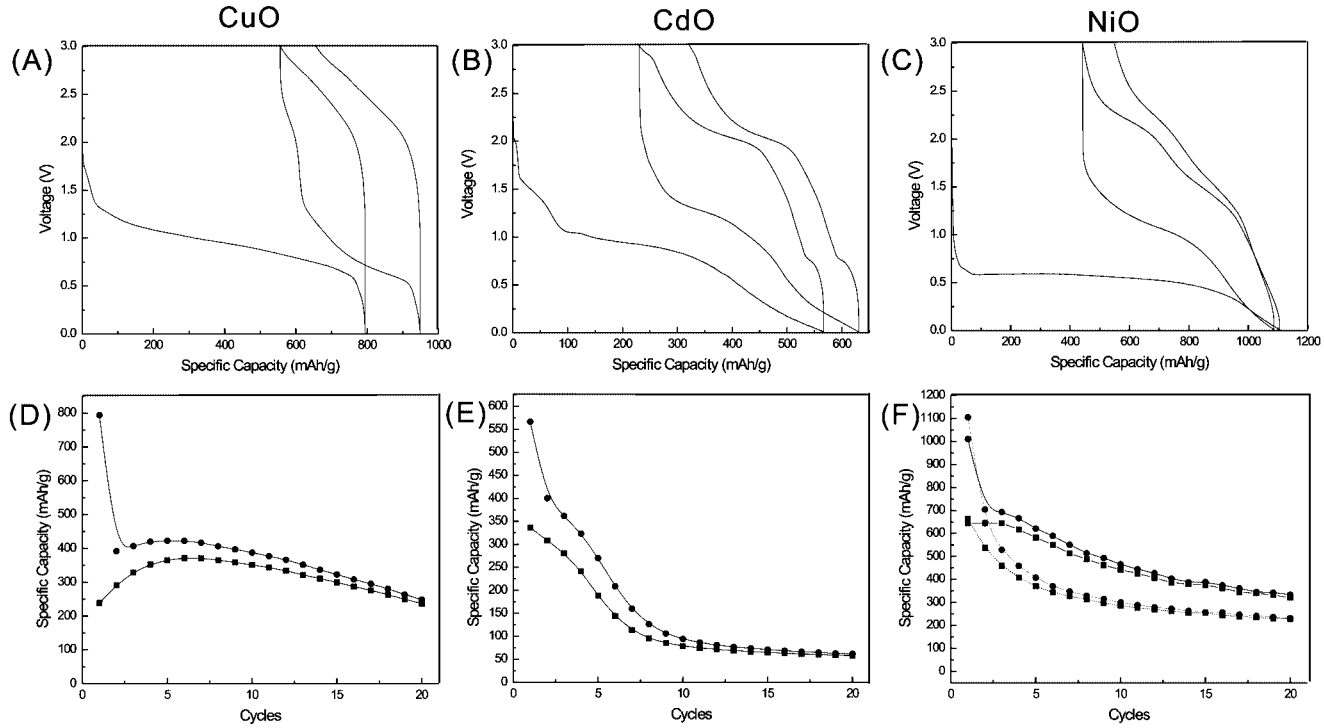

Figure 10. Battery testing results of our synthesized CuO, CdO, and NiO nanostructures. (A−C) Discharge/charge curves of the first two cycles. (D−F) Discharge (●) and charge (■) capacities as a function of cycle numbers. In F, the upper curves are the capacity curves for thin nanoplates (thickness <100 nm) while the lower curves are the capacity curves for thick nanoplates (thickness ~1 μm). For all the measurements, the current rate is 111 mA/g.

a gradual slope and moves up to 1.2−0.8 V. This implies that an irreversible change in our material occurs in the first cycle whose nature is still not well-known[29b] and that might be due to the pulverization of the electrode materials in the first discharge. We also tried to compare the cycleability of the NiO nanoplates with different thicknesses and found that cells based on the thinner nanoplates show a better performance with less capacity decay. After 20 cycles, the <100 nm thin nanoplates still have a capacity of 350 mA h/g, which is 100 mA h/g larger than that of the 1 μm thick sample (Figure 10F, the upper two curves vs the lower two curves). This result shows that nanoplate stacking is detrimental to battery performance in that the aggregate would retard the Li^+ ion diffusion.

Conclusion

We have developed a general and facile synthetic method for metal hydroxide/oxide nanostructures based on the ammonia-evaporation-induced hydrolysis of metal−ammonia complex ions. Ammonia molecules play multiple roles in our synthesis. They form stable complex ions with metal cations at the beginning. During the reaction, the continuous evaporation of ammonia induces the hydrolysis of the complex ions to form the primary nanoparticles. They grow in a dynamic environment with the continuous decrease of the pH and the ammonia concentration in the solution. The pH controls the charges carried by the particles while the ammonia molecules can passivate the surface and thereby influence the growth and aggregation behaviors of the particles. As a result, at high ammonia concentration and pH, the formed particles are stable in the solution, corresponding to the "incubation" period. With the gradual decrease of pH and ammonia concentration, the primary particles attach with each other and form the various hierarchical nanostructures, including the CuO spheres with radiating nanoplates, the densely branched ZnO nanowires, and the $Cd(OH)_2$ nanobundles. In addition to the synthesis and mechanism studies, we have also investigated the electrochemical reactivity of CuO spheres, CdO nanofibers, and NiO nanoplates with lithium and demonstrated their potential application as anode materials for lithium ion batteries.

Summary

Hierarchical CuO spheres with radiating nanoplates, densely branched ZnO nanowires, $Cd(OH)_2$ nanofibers, and $Ni(OH)_2$ nanoplates prepared through an ammonia-evaporation-induced method.

Supporting Information Available: Solution pH and nanostructure morphological evolution with reaction time for the Cu and Zn systems, SEM images of ZnO precipitates and floating films, XRD pattern of the ZnO branched structure, SEM images of NiO nanoplates after annealing, and SEM image of CuO spheres after five cycles (PDF). This material is available free of charge via the Internet at http://pubs.acs.org.

CM070784G